Predicting Frictional Properties of Graphene Kirigami Using Molecular Dynamics and Neural Networks

Designs for a negative friction coefficient.

Mikkel Metzsch Jensen

Predicting Frictional Properties of Graphene Kirigami Using Molecular Dynamics and Neural Networks

Designs for a negative friction coefficient.

Mikkel Metzsch Jensen

Predicting Frictional Properties of Graphene Kirigami Using Molecular Dynamics and Neural Networks

Abstract

Abstract.

Acknowledgments

Acknowledgments.

iv

List of Symbols

F_N Normal force (normal load)

Acronyms

FFM Friction Force Microscopes. 7

FK Frenkel-Kontorova. 7

LJ Lennard-Jones. 7, 8, 9

MD Molecular Dynamics. 1, 2, 3, 7, 8, 16, 19, 20, 21

ML Machine Learning. 2, 3, 21

Contents

Chapter 1

Introduction

1.1 Motivation

Friction is the force that prevents the relative motion of objects in contact. Even though the everyday person might not be familiar with the term *friction* we recognize it as the inherent resistance to sliding motion. Some surfaces appear slippery and some rough, and we know intuitively that sliding down a snow-covered hill is much more exciting than its grassy counterpart. Without friction, it would not be possible to walk across a flat surface, lean against the wall without falling over or secure an object by the use of nails or screws [p. 5] [1]. It is probably safe to say that the concept of friction is integrated into our everyday life to such an extent that most people take it for granted. However, the efforts to control friction date back to the early civilization (3500 B.C.) with the use of the wheel and lubricants to reduce friction in translational motion [2]. Today, friction is considered a part of the wider field *tribology* derived from the Greek word *Tribos* meaning "rubbing" and includes the science of friction, wear and lubrication [2]. The most compelling motivation to study tribology is ultimately to gain full control of friction and wear for various technical applications. Especially, reducing friction is of great interest as this has tremendous advantages for energy efficiency. It has been reported that tribological problems have a significant potential for economic and environmental improvements [3]:

> "On global scale, these savings would amount to 1.4% of the GDP annually and 8.7% of the total energy consumption in the long term." [4].

On the other hand, the reduction of friction is not the only sensible application for tribological studies. Controlling frictional properties, besides minimization, might be of interest in the development of a grasping robot where finetuned object handling is required. While achieving a certain "constant" friction response is readily obtained through appropriate material choices, we are yet to unlock the full capabilities to alter friction dynamically on the go. One example from nature inspiring us to think along these lines are the gecko feet. More precisely, the Tokay gecko has received a lot of attention in scientific studies aiming to unravel the underlying mechanism of its "togglable" adhesion properties. Although geckos can produce large adhesive forces, they retain the ability to remove their feet from an attachment surface at will [5]. This makes the gecko able to achieve a high adhesion on the feet when climbing a vertical surface while lifting them for the next step remains relatively effortless. For a grasping robot, we might consider an analog frictional concept of a surface material that can change from slippery to rough on demand depending on specific tasks; Slippery and smooth when interacting with people and rough and firmly gripping when moving heavy objects.

In recent years an increasing amount of interest has gone into the studies of the microscopic origin of friction, due to the increased possibilities in surface preparation and the development of nanoscale experimental methods. Nano-friction is also of great concern for the field of nano-machining where the frictional properties between the tool and the workpiece dictate machining characteristics [3]. With concurrent progress in computational capacity and development of Molecular Dynamics (MD), numerical investigations serve as an invaluable tool for getting insight into the nanoscale mechanics associated with friction. This simulation-based approach can be considered as a "numerical experiment" enabling us to create and probe a variety of high-complexity systems which are still out of reach for modern experimental methods.

In materials science such MD-based numerical studies have been used to explore the concept of so-called *metamaterials* where material compositions are designed meticulously to enhance certain physical properties [6–

11]. This is often achieved either by intertwining different material types or removing certain regions completely. In recent papers by Hanakata et al. [6, 7] numerical studies have showcased that the mechanical properties of a graphene sheet, yield stress and yield strain, can be altered through the introduction of so-called *kirigami* inspired cuts into the sheet. Kirigami is a variation of origami where the paper is cut additionally to being folded. While these methods originate as an art form, aiming to produce various artistic objects, they have proven to be applicable in a wide range of fields such as optics, physics, biology, chemistry and engineering [12]. Various forms of stimuli enable direct 2D to 3D transformations through folding, bending, and twisting of microstructures. While original human designs have contributed to specific scientific applications in the past, the future of this field is highly driven by the question of how to generate new designs optimized for certain physical properties. However, the complexity of such systems and the associated design space make for seemingly intractable problems ruling out analytic solutions.

Earlier architecture design approaches such as bioinspiration, looking at gecko feet for instance, and Edisonian, based on trial and error, generally rely on prior knowledge and an experienced designer [9]. While the Edisonian approach is certainly more feasible through numerical studies than real-world experiments, the number of combinations in the design space rather quickly becomes too large for a systematic search, even when considering the computation time on modern-day hardware. However, this computational time constraint can be relaxed by the use of machine learning (ML) which has proven successful in the establishment of a mapping from the design space to physical properties of interest. This gives rise to two new styles of design approaches: One, by utilizing the prediction from a trained network we can skip the MD simulations altogether resulting in an *accelerated search* of designs. This can be further improved by guiding the search accordingly to the most promising candidates, for instance, as done with the *genetic algorithm* based on mutation and crossing of the best candidates so far. Another more sophisticated approach is through generative methods such as *Generative Adversarial Networks* (GAN) or diffusion models with the latter being used in state-of-the-art AI systems such as OpenAI's DALL·E2 or Midjourney SOURCE?. By working with a so-called *encoder-decoder* network structure, one can build a model that reverses the prediction process. That is, the model predicts a design from a set of physical target properties. In the papers by Hanakata et al both the *accelerated search* and the *inverse design* approach was proven successful to create novel metamaterial kirigami designs with the graphene sheet.

Hanakata et al attribute the variety in yield properties to the non-linear effects arising from the out-of-plane buckling of the sheet. Since it is generally accepted that the surface roughness is of great importance for frictional properties it can be hypothesized that Kirigami-induced out-of-plane buckling can also be exploited for the design of frictional metamaterials. For certain designs, we might hope to find a relationship between the stretching of the sheet and frictional properties. If significant, this could give rise to an adjustable friction behavior beyond the point of manufacturing. For instance, the grasping robot might apply such a material as artificial skin for which stretching or relaxing of the surface could result in a changeable friction strength.

In addition, the Kirigami graphene properties can be explored through a potential coupling between the stretch and the normal load, through a nanomachine design, with the aim of altering the friction coefficient. This invites the idea of non-linear friction coefficients which might in theory also take on negative values. The latter would constitute a rarely found property which is mainly found for the unloading phase of adhesive surfaces [13] or for the loading phase of particular heterojunction materials [14, 15]

To the best of our knowledge, Kirigami has not yet been implemented to alter the frictional properties of a nanoscale system. However, in a recent paper by Liefferink et al. [16] it is reported that macroscale kirigami can be used to dynamically control the macroscale roughness of a surface through stretching. They reported that the roughness change led to a changeable frictional coefficient by more than one order of magnitude. This supports the idea that Kirigami designs can be used to alter friction, but we believe that taking this concept to the nanoscale regime would involve a different set of underlying mechanisms and thus contribute to new insight in this field.

1.2   Goals

In this thesis, we investigate the possibility to alter the frictional properties of a graphene sheet through the application of Kirigami-inspired cuts and stretching of the sheet. With the use of molecular dynamics (MD) simulations, we evaluate the frictional properties of various Kirigami designs under different physical conditions. With the use of machine learning (ML), we perform an accelerated search of designs to explore new designs. The main goals of this thesis can be summarized as follows.

1. Design an MD simulation procedure to evaluate the frictional properties of a Kirigami graphene sheet under specified physical conditions.

2. Develop a numerical framework for creating various Kirigami designs, both by seeking inspiration from macroscale designs and by the use of a random walk based algorithm.

3. Investigate the frictional behavior under varying load and stretch for different Kirigami designs.

4. Develop and train an ML model to predict the MD simulation result and perform an accelerated search of new designs for the scope of optimizing certain frictional properties.

1.3 Contributions

What did I actually achieve Include Githib link

1.4 Thesis structure

In Part I: Background Theory, we cover the theoretical background related to Friction (**??**), Molecular Dynamics (Chapter 2) and Machine Learning (**??**).

In **??**: Friction, we introduce the most relevant theoretical concepts of friction through a division by scale: Macroscale (**??**), Microscale (**??**) and nanoscale (**??**). We emphasize the nanoscale since this is of the most importance for our study. This is followed by a summary of relevant experimental and numerical results **??** and a more formal specification of our research questions (**??**).

In Chapter 2: Molecular Dynamics, we introduce the main concepts related to the simulations used in this thesis. The main parts involve a description of the potentials used (Sec. 2.1), the numerical solutions (Sec. 2.2) and the modeling of temperature (Sec. 2.3)

In **??**: Machine Learning, we introduce the basics of machine learning through a general presentation of the neural network **??** followed by the convolutional network (**??**) which we will use in our study. Additionally, we discuss a strategy for choosing model hypertuning (**??**) and a simple approach for model prediction explanations (). Finally, we introduce a version of the genetic algorithm applicable for accelerated search based on a machine learning model (**??**).

In Part II: Simulations, we define our numerical procedure and present and discuss the main findings of this thesis.

In **??**: System, we ...

In **??**: Pilot study, we ...

In **??**: XXX ...

In **??**: XXX, ...

The thesis is summarized in Chapter 3

Additional figures are shown in **??**, **??** and **??**. get appendix with only letter A., B. and C.

Part I

Background Theory

Chapter 2

Molecular Dynamics

Molecular Dynamics (MD) is an atomistic simulation method that is commonly employed in the investigation of atomic-scale friction due to its ability to track each atom in a system [17]. Due to advances in computing algorithms and hardware, MD simulations have become increasingly capable of simulating tribological systems in recent years [18]. We will utilize MD as our primary numerical approach to simulate and examine the effect of nanoscale kirigami in our system. Such small-scale modifications are still beyond the reach of experimental approaches, and the complexity of the system precludes analytical solutions as well. Hence, MD simulations represent one of the few viable options for addressing this problem.

An MD simulation can be viewed as a "computational experiment", where we specify a set of initial conditions and evolve the system to measure certain properties of interest. This is done through the definition of interatomic force fields which allows us to solve Newton's equation of motion by numerical integration [19, p. 303]. Other more sophisticated and accurate approaches exist, like Ab initio MD which utilizes electronic structure calculations at simulation time [20]. One of the most popular methods is based on density functional theory (DFT) [21] which considers quantum mechanical modeling of the electronic state of the system. However, such methods are rarely used in sliding friction since the computational cost makes it only feasible to handle relatively small systems, typically hundreds of atoms, for relatively short durations, typically much less than 1 ns [22]. In addition, we aim to perform multiple simulations under the change of various parameters which put additional pressure on the computational resources.

In this chapter, we will introduce the fundamental principles behind MD modeling and describe our implementation choices with respect to our system of interest. Our primary objective is to establish a functional simulation that can be used to explore nanoscale friction, so our discussion is focused on the key aspects of the method rather than a comprehensive analysis of all available techniques.

2.1 Potentials

The interatomic force field governing the MD simulation is derived from the choice of potentials. The selection of potentials has a significant impact on the outcomes obtained. The potentials can vary from intricate energy surfaces that consider electrons at either the density-functional or tight-binding level to angle-dependent many-particle potentials, basic pairwise potentials, or simple models of elastic springs, and extensions of FK-type formulations [22]. For the choice of potentials, and materials, we take a basis in the numerical MD study by Li et al. [23] simulating a FFM type setup where a Si tip indents a graphene sheet supported by a Si substrate. It is evident that the experimental arrangement utilized by Li et al. varies from our system since they impose a Silicon tip on a graphene sheet that is supported by a Silicon substrate, whereas we will be sliding the entire sheet upon the substrate. Nevertheless, we contend that this should serve as an appropriate starting point for selecting the potential setup. We describe the covalent bonds between carbon atoms C-C in the graphene sheet and between silicon atoms Si-Si in the substrate by the Tersoff and Stillinger–Weber potentials, respectively. A typical 12–6 Lennard–Jones (LJ) potential is used to describe the van der Waals adhesive interaction between the graphene sheet and the substrate.

2.1.1 General formulation of potentials

The physical potential governing the mechanics of the atomic system can generally be thought of as an n-body expansion in order of participating atoms as

$$E = \sum_i V_1(\mathbf{r}_i) + \sum_{\substack{i,j \\ i<j}} V_2(\mathbf{r}_i, \mathbf{r}_j) + \sum_{\substack{i,j,k \\ i<j<k}} V_3(\mathbf{r}_i, \mathbf{r}_j, \mathbf{r}_i) + \cdots,$$

where $\mathbf{r}_n$ is the position of the nth particle and V_m is called an m-body potential [24]. The first one-body term corresponds to an external potential (e.g. gravity), followed by the two-body term, the three-body term and so on. The simplest model that includes particle interaction is the pair potential truncating the expansion after the two-body term. A general feature of the pair potentials is that they favor close-packed structures that are unsuited to describe covalent bonds that take more open structures. In particular, pair potentials are completely inapplicable to strongly covalent systems [24]. In order to accommodate the description of covalent bonds we can include the next step of the expansion, which involves the three-body that is used in both the Stillinger–Weber potential for Si-Si bonds and the Tersoff potential for the C-C bonds. For the interaction between the sheet and the substrate, we use the LJ pair potential describing the non-bonded van der Waals interaction which is often used to treat interactions between surfaces in friction simulations [3, 25–27]. In the following sections Sec. 2.1.2 to 2.1.4 we will introduce each of the potentials in more detail.

2.1.2 Lennard Jones

TODO: Add potential curve figure

The theoretical basis in this subsection is based on [28–30]. The Lennard-Jones (LJ) model is probably one of the most commonly used pair potentials for MD simulations. LJ models the potential energy between two non-bonding atoms solely based on interatomic distance. The model accounts for long-ranged attractive forces arising from London dispersion forces (dipole-induced dipole)and repulsive forces that capture the hard core of overlapping electron orbitals at small distances (Pauli repulsion). Thus, it assumes neutrally charged atoms and was originally proposed for noble gases. The classical 12–6 version of the model, referring to the powers of the repulsive and attractive forces respectively, reads

$$E = 4\epsilon \left[\left(\frac{\sigma}{r} \right)^{12} - \left(\frac{\sigma}{r} \right)^6 \right], \qquad r < r_c, \tag{2.1}$$

where r is the interatomic distance with cut-off r_c, ϵ is the depth of the potential well and σ the interatomic distance where the the potential is zero. The potential is sketched in Fig. 2.1

By solving for the potential minimum ($dE/dr = 0$) we find the equilibrium distance to be $r_0 = \sigma 2^{1/6}$. This makes for a slightly more intuitive interpretation of σ as the parameter which sets the equilibrium distance between atoms, i.e. the dividing line for which the force is repulsive or attractive. We will adopt the potential parameters from Li et al. [23] with $\sigma = 3.0\,\text{Å}$ and $\epsilon = 0.0092\,\text{eV}$.
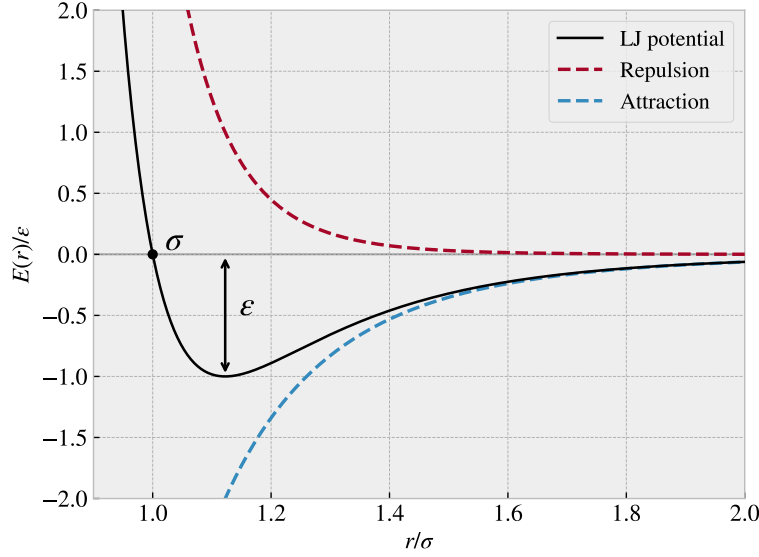
Figure 2.1: Caption

2.1.3 Stillinger-Weber

The theoretical background of this subsection is based on [31, 32]. The Stillinger-Weber potential takes the form of a three-body potential

$$E = \sum_i \sum_{j>i} \phi_2(r_{ij}) + \sum_i \sum_{j \neq i} \sum_{k>j} \phi_3(r_{ij}, r_{ik}, \theta_{ijk}),$$

where r_{ij} denotes the distance between atom i and j, and θ_{ijk} the angle between bond ij and jk (see Fig. 2.2). The summation is over all neighbors j and k of atom i within a cut-off distance $r = a\sigma$.
The two-body term ϕ_2 builds from the LJ model with the addition of an exponential cutoff term

$$\phi_2(r_{ij}) = A_{ij}\epsilon_{ij} \left[B_{ij} \left(\frac{\sigma_{ij}}{r_{ij}} \right)^{p_{ij}} - \left(\frac{\sigma_{ij}}{r_{ij}} \right)^{q_{ij}} \right] \exp(\frac{\sigma_{ij}}{r_{ij} - a_{ij}\sigma_{ij}}). \tag{2.2}$$

The model parameters A, ϵ, B, σ, p, q and a come with i,j indices to indicate that these parameters should be specified for each unique pair of atom types. However, in our case, we will only provide a single value for each model parameter as we are exclusively dealing with Si-Si bonds. We see that the first term in Eq. (2.2) is reminiscent of the LJ model in Eq. (2.1) while the last term effectively drives the potential to zero at $r = a\sigma$, which is the chosen cut-off distance for the potential evaluation. With the chosen model parameters for the Si-Si modeling, see Table 2.1, the cut-off becomes ~ 3.8 Å. The three body term includes an angle dependency as

$$\phi_3(r_{ij}, r_{ik}, \theta_{ijk}) = \lambda_{ijk} \ \epsilon_{ijk} \left[\cos\theta_{ijk} - \cos\theta_{0,ijk} \right]^2 \exp(\frac{\gamma_{ij}\sigma_{ij}}{r_{ij} - a_{ij}\sigma_{ij}}) \exp(\frac{\gamma_{ik}\sigma_{ik}}{r_{ik} - a_{ik}\sigma_{ik}}), \tag{2.3}$$

where $\theta_{0,ijk}$ is the equilibrium angle. The first term of Eq. (2.3) includes an angle dependency analog to a harmonic oscillator based on a cosine angle distance from the equilibrium angle. The final two terms act again as a cut-off function by driving the potential to zero at $r_{ij} = a_{ij}\sigma_{ij}$ and $r_{ik} = a_{ik}\sigma_{ik}$ respectively. We adopt the parameters for Si-Si suggested in the original paper by Stillinger and Weber [32] which is shown in Table 2.1 along with an interpretation of each model parameter.
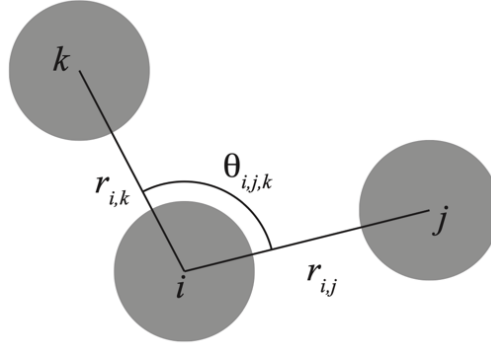
Figure 2.2: Caption

Table 2.1: Parameters for the Stilliner-Weber potential used for intermolecular interactions in the silicon substrate. The parameters are adopted from [32].

Parameter	Value	Description
ϵ	2.1683	Individual depth of the potential well for each pair and triplets of atom types.
σ	2.0951	Distance for which the individual pair interactions has zero potential (analog to the LJ model).
a	1.80	The individual cut-off distance for each pair of atom types.
λ	21.0	The overall depth of the three-body potential well.
γ	1.20	The shape of the three-body cut-off terms.
$\cos(\theta_0)$	-1/3	Cosine of equilibrium angle.
A	7.049556277	The overall depth of the two-body potential well.
B	0.6022245584	Scales the repulsion part of the two-body term.
p	4.0	The power dependency for the repulsion part of the two-body term.
q	0.0	The power dependency for the attraction part of the two-body term.
tol	0.0	(LAMMPS specific) Option to define a different cut-off than the theoretical $r = a\sigma$. $tol = 0$ refers to the use of the theoretical.

2.1.4 Tersoff

The theoretical basis in this subsection is based on [24, 33]. The Tersoff potential abandons the idea of a general n-body form and attempts instead to build the model on a more physics-informed approach; The more neighbors an atom has the weaker the bonds will be. Thus, it introduces the bond order (bond strength), which is environment specific and decreases with increasing bond coordination (number of neighbors for a given atom). A sketch of the Tersoff potential can be seen in [**fig:bond˙order**]. The potential energy is taken to have the form

$$E = \sum_i E_i = \frac{1}{2} \sum_{i \neq j} V_{ij},$$

$$V_{ij} = f_C(r_{ij}) \big[f_R(r_{ij}) + b_{ij} f_A(r_{ij}) \big],$$

where the total potential energy E is decomposed into a bond energy V_{ij}. The indices i and j run over the atoms of the system with r_{ij} denoting the distance between atom i and j. Notice that the sum includes all combinations of i, j but $i \neq j$, meaning that an atom cannot bond to itself. However, we count other bonds twice, e.g. $(1, 2)$ and $(2, 1)$, which is the explanation for the additional factor $1/2$. The reasoning for the double counting lies in the asymmetry of the bond order $b_{ij} \neq b_{ji}$ leading to $V_{ij} \neq V_{ji}$. The bond energy is composed of

a repulsive term f_R, arising from overlapping wave functions, and an attractive term f_A associated with bonding. f_C is simply a smooth cut-off function to increase computational efficiency. b_{ij} represent the bond order, i.e. the strength of the bonds, which depends inversely on the number of bonds, the bond angles (θ_{ijk}) and optionally the relative bond lengths (r_{ij}, r_{jk}). Notice that an additional cut-off term a_{ij} was originally multiplied to f_R as a way of including terms that limit the range of the interactions to the first neighbor shell. This kind of limitation is already included in b_{ij} for the attractive term f_A but is often omitted for the repulsive term f_R, and we do so as well by setting $a_{ij} = 1$.

The cut-off function f_C goes from 1 to 0 over a small interval range $R \pm D$ as

$$f_C(r) = \begin{cases} 1 & r < R - D \\ \frac{1}{2} - \frac{1}{2}\sin\left(\frac{\pi}{2}\frac{r-R}{D}\right) & R - D < r < R + D \\ 0 & r > R + D \end{cases},$$

which is continuous and differentiable for all r. R is usually chosen to include only the first neighbor shell. The repulsive and attractive terms f_R and f_A are modeled as an exponential function, similar to a Morse potential,

$$f_R(r) = A\exp(-\lambda_1 r),$$
$$f_A(r) = -B\exp\left(-\lambda_2 r\right).$$

The novel feature of the Tersoff model lies in the modeling of the bond order b_{ij} which includes three-body interactions by summing over a third atom $k \neq i, j$ within the cut-off $r_{ik} < R + D$ as shown in the following.

$$b_{ij} = \left(1 + \beta^n \zeta_{ij}^n\right)^{-\frac{1}{2n}} \tag{2.4}$$

$$\zeta_{ij} = \sum_{k \neq i,j} f_C(r_{ik}) g\left(\theta_{ijk}(r_{ij}, r_{ik})\right) \exp\left(\lambda_3{}^m (r_{ij} - r_{ik})^m\right) \tag{2.5}$$

$$g(\theta) = \gamma_{ijk}\left(1 + \frac{c^2}{d^2} - \frac{c^2}{\left[d^2 + (\cos\theta - \cos\theta_0)^2\right]}\right). \tag{2.6}$$

In Eq. (2.6) $\zeta_{i,j}$ is an effective coordination and $g(\theta)$ captures angle dependency as it is minimized at the equilibrium angle $\theta = \theta_0$. The parameters used to model the graphene C-C bonds are adopted from J. Tersoff [34] and summarized in Table 2.2.
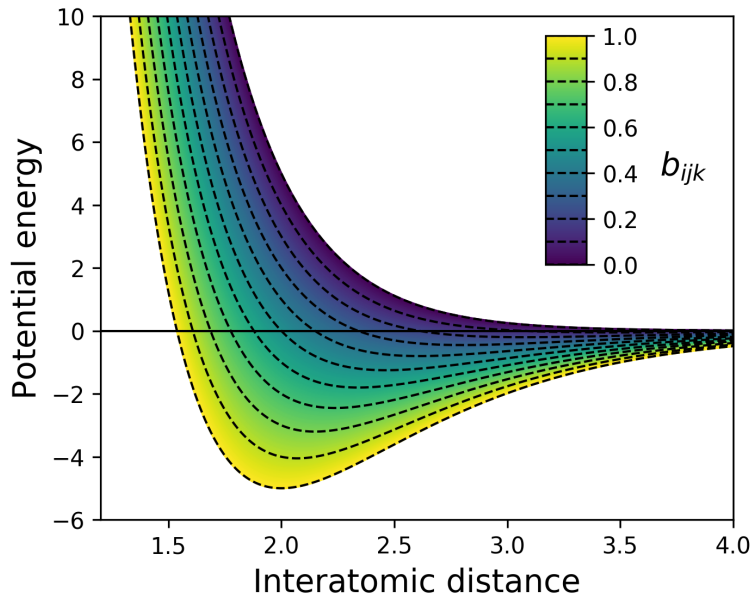

Figure 2.3: Caption [35]

Table 2.2: Parameters for the Tersoff potential used for intermolecular interations in the graphene sheet

Parameter	Value	Description
R	1.95 Å	Center distance for cut-off.
D	0.15 Å	Thickness of cut-off region.
λ_1	3.4879 Å^{-1}	Decay of repulsion potential term f_R.
λ_2	2.2119 Å^{-1}	Decay of attractive potential term f_A.
A	1393.6 eV	Repulsion potential maximum at the core ($f_R(r_{ij} = 0)$).
B	346.74 eV	Attractive potential minimum at core ($f_A(r_{ij} = 0)$).
β	1.5724×10^{-7}	Base for the exponetial scaling of the effective coordination effect on bond strength b_{ij}.
n	0.72751	Power law exponent for the bond order dependency.
λ_3	0.0 Å^{-1}	Base for the exponential cut-off of the effective coordination $\zeta_{i,j}$.
m	—	Exponent for the exponential cut-off of the effective coordination $\zeta_{i,j}$. Not relevant since $\lambda_3 = 0$.
γ	1.0	Linear scaling of the angle dependecny term.
c	3.8049×10^4	Strength of the angular effect.
d	4.3484	Determines the "sharpness" of the angular dependency.
$\cos(\theta_0)$	-0.57058	Cosine of the equilibrium angle.

2.2   Integration

Assuming that one has defined a system of particles, setting the atom types, initial positions and velocities, and interatomic potentials, we need to move the system forward in time. By solving Newton's equations of motion we achieve this by effectively sampling the microcanonical ensemble characterized by a constant number of particles N, volume V and energy E, hence denoted NVE [36]. Newtons equations of motion read

$$m_i \frac{d^2 \mathbf{r}_i}{dt^2} = \mathbf{F}_i = -\nabla U_i, \tag{2.7}$$

where i is the particle index, m_i its mass, $\mathbf{r}_i = (x_i, y_i, z_i)$ the position, t is time, $\nabla_i = (\frac{\partial}{\partial x_i}, \frac{\partial}{\partial y_i}, \frac{\partial}{\partial z_i})$ and U_i the potential energy. The potential energy is defined by the interatomic potentials and any external forces applied to the system. Since the forces defined by the potentials are conservative we expect the energy of the solution to be conserved. We can redefine Eq. (2.7) in terms of two coupled first order differential equations

$$\dot{\mathbf{v}}_i(t) = \frac{\mathbf{F}}{m_i}, \qquad \dot{\mathbf{r}}_i(t) = \mathbf{v}_i(t), \tag{2.8}$$

where $\dot{x} = dx/dt$ is Newton's notation for the time derivative and $\mathbf{v} = (v_x, v_y, v_z)$ is velocity. Numerically we can solve the coupled equations by integrating over discrete timesteps. That is, we discretize the solution into temporal steps $t_k = t_0 + k\Delta t$ with start time t_0 and time-step Δt. The choice of timestep should be chosen small enough to avoid instabilities in the simulation.

2.2.1   Velocity Verlet

A popular approach to the numerical integration of Newton's equations of motion, when written as two coupled first-order differential equations Eq. (2.8), is the *velocity verlet* algorithm. We can derive the algorithm by the use of Taylor expansions. We begin by expanding the next-step position vector $\mathbf{r}_i(t + \Delta t)$ at time t

$$\mathbf{r}_i(t + \Delta t) = \mathbf{r}_i(t) + \dot{\mathbf{r}}_i(t)\Delta t + \frac{\ddot{\mathbf{r}}_i(t)}{2}\Delta t^2 + \mathcal{O}(\Delta t^3), \tag{2.9}$$

where $\ddot{\mathbf{r}} = d^2\mathbf{r}/dt^2$ and Δt^n is simply the relaxed notation for $(\Delta t)^n$. Thus, the remaining $\mathcal{O}(\Delta t^3)$ term is big O notation for the truncation including a dependence of Δt^3 and higher order. Similarly, we take the expansions of

the next-step velocity vector $\mathbf{v}_i(t + \Delta t)$ at time t

$$\mathbf{v}_i(t + \Delta t) = \mathbf{v}_i(t) + \dot{\mathbf{v}}_i(t)\Delta t + \frac{\ddot{\mathbf{v}}_i(t)}{2}\Delta t^2 + \mathcal{O}(\Delta t^3). \tag{2.10}$$

Finally, by taking the expansion of $\dot{\mathbf{v}}_i(t + \Delta t)$ we can eliminate the $\ddot{\mathbf{v}}_i$-term in Eq. (2.10) and simplify it as shown in the following.

$$\dot{\mathbf{v}}_i(t + \Delta t) = \dot{\mathbf{v}}_i(t) + \ddot{\mathbf{v}}_i(t)\Delta t + \mathcal{O}(\Delta t^2)$$

$$\frac{\ddot{\mathbf{v}}_i(t)}{2}\Delta t^2 = \frac{\Delta t}{2}\Big(\dot{\mathbf{v}}(t + \Delta t) - \dot{\mathbf{v}}_i(t)\Big) + \mathcal{O}(\Delta t^3)$$

$$\Downarrow$$

$$\mathbf{v}_i(t + \Delta t) = \mathbf{v}_i(t) + \dot{\mathbf{v}}_i(t)\Delta t + \frac{\Delta t}{2}\Big(\dot{\mathbf{v}}_i(t + \Delta t) - \dot{\mathbf{v}}_i(t)\Big) + \mathcal{O}(\Delta t^3)$$

$$= \mathbf{v}_i(t) + \frac{\Delta t}{2}\Big(\dot{\mathbf{v}}_i(t) + \dot{\mathbf{v}}_i(t + \Delta t)\Big) + \mathcal{O}(\Delta t^3). \tag{2.11}$$

By combining Eq. (2.9) and Eq. (2.11), and $\dot{\mathbf{v}} = \mathbf{F}_i(t)/m_i$ and $\mathbf{v} = \dot{\mathbf{r}}$ we arrive at the final scheme

$$\mathbf{r}_i(t + \Delta t) = \mathbf{r}_i(t) + \mathbf{v}_i(t)\Delta t + \frac{\mathbf{F}_i(t)}{2m_i}\Delta t^2 + \mathcal{O}(\Delta t^3),$$

$$\mathbf{v}_i(t + \Delta t) = \mathbf{v}_i(t) + \frac{\mathbf{F}_i(t) + \mathbf{F}_i(t + \Delta t)}{2m_i}\Delta t + \mathcal{O}(\Delta t^3).$$

This scheme will give a local error on the order Δt^3 corresponding to a global error of Δt^2. One of the most popular ways to implement this numerically is as stated in the following steps.

1. Calculate $v_{k+\frac{1}{2}} = v_k + \frac{F_k}{2m}\Delta t$.

2. Calculate $r_{k+1} = r_k + v_{k+\frac{1}{2}}\Delta t$.

3. Evaluate the force $F_{k+1} = F(r_{k+1})$.

4. Calculate $v_{k+1} = v_{k+\frac{1}{2}} + \frac{F_{k+1}}{2m}\Delta t$

2.3 Thermostats

In **??** we introduced friction as an ultimate result of the equipartition theorem stating that the kinetic energy supplied by the sliding motion will tend to transfer to other degrees of freedom and eventually dissipate to the environment as heat through phonon transport (and electrons for a metallic system) [18]. However, when modeling the system exclusively through the solutions of Newton's equations of motion we have no dissipation channel in our system. Instead, the energy will reflect back and forth and eventually "pile up" in the system in an unphysical manner. In order to resolve this issue we have to include the environment in our modelling by adding some kind of heatsink that allows for heat dissipation. This can be approached in a variety of ways, but one of the more common choices, which we will use as well, is the Langevin thermostat.

2.3.1 Langevin thermostat

The Langevin thermostat is a stochastic thermostat that modifies Newton's equation of motion such that the solution lies in the canonical ensemble characterized by a constant number of particles N, constant volume V and constant temperature T, hence denoted NVT [18]. When going from the microcanonical ensemble NVE, described by Newton's equation of motion Eq. (2.7), to the canonical ensemble NVT, we effectively perform a Legendre transformation which substitutes temperature for energy in the regard to which variables are held constant. The canonical ensemble system is represented by a finite system being in contact with an infinite heat bath of temperature T. The NVT ensemble is equivalent to sampling a system in thermodynamic equilibrium where the weight of each microscopic state is given by the Boltzmann factor $\exp[-E/(k_BT)]$ where k_B is the Boltzmann constant.

The Langevin thermostat is governed by the Langevin equation which originated as the modified version of Newton's equations for a Brownian particle [37]. A Brownian particle is a small particle suspended in liquid, e.g. pollen or dust, named after Robert Brown (1773–1858) who was the first to observe its jittery motion. The Langevin equation describes this motion as the combination of viscous drag force $-\alpha\mathbf{v}$, where α is a positive friction coefficient and $\mathbf{v}$ the velocity vector, and a random fluctuation force $\mathbf{R}$. The Langevin equation reads

$$m\frac{d\mathbf{v}}{dt} = -\alpha\mathbf{v} + \mathbf{R}, \tag{2.12}$$

where m is the particle mass. This effectively describes the particle of interest, the Brownian particle, as being suspended in a sea of smaller particles. The collision with these smaller particles is modeled by the combined effects of a drag force and a fluctuation force. If the fluctuation force is excluded Eq. (2.12) becomes

$$m\frac{d\mathbf{v}}{dt} = -\alpha\mathbf{v} \quad \Rightarrow \quad \mathbf{v}_i(t) = v(0)e^{-\frac{\alpha t}{m}},$$

where the solution shows that the Brownian particle will come to a complete stop after a long time $\mathbf{v}_i(t \to \infty) \to \mathbf{0}$. This is in violation with the equipartition theorem which dictates a non-zero average squared velocity in equilibrium $\langle v^2 \rangle_{\text{eq}}$ as

$$\frac{1}{2}m\langle v^2 \rangle_{\text{eq}} = \frac{k_B T}{2}. \tag{2.13}$$

Hence, the fluctuation force is necessary to obtain the correct equilibrium. In the following, we will introduce the reasoning behind the Langevin equations in one dimension in order to simplify the notation a bit [37].

We describe the statistical nature of the collisions as a sum of independent momentum transfers

$$\Delta P = \sum_i^N \delta p_i,$$

where ΔP denotes the change of momentum after N momentum transfers δp_i from the environment to the Brownian particle. We assume the first and second moments to be $\langle \delta p \rangle = 0$ and $\langle \delta p \rangle = \sigma^2$. When N is large the central limit theorem states that the random variable ΔP has a gaussian distribution with $\langle P \rangle = 0$ and $\langle \Delta P^2 \rangle = N\sigma^2$. If we consider the momentum change ΔP over a discrete time Δt, where the number of collisions is proportional to time $N \propto \Delta t$, the corresponding fluctuation force $R = \Delta P/\Delta t$ will have a variance

$$\langle R^2 \rangle = \frac{\langle \Delta P^2 \rangle}{\Delta t^2} = \frac{N\sigma^2}{\Delta t^2} \propto \frac{1}{\Delta t}.$$

In a computer simulation, we pick a random force $R(t)$ from a Gaussian distribution every time-step Δt. These forces will not be correlated as long as Δt is larger than the correlation time of the forces from the molecules. By assuming that this criterion is met we can write the correlation function as

$$\langle R(t)R(0) \rangle = \begin{cases} \frac{a}{\Delta t}, & |\Delta t| < \Delta t/2 \\ 0, & |\Delta t| > \Delta t/2, \end{cases} \tag{2.14}$$

where the constant a describes the magnitude of the fluctuations. We could in principle determine a from the variance of ΔP, but instead, we will determine it from the equipartition principle. In the limit $\Delta t \to 0$ the correlation function becomes

$$\langle R(t)R(0) \rangle = a\delta(t), \tag{2.15}$$

where δ denotes the Dirac delta function. This is valid for all spatial coordinates which are all independent of each other. Since both the drag force and the fluctuation force originate from the molecular fluid, where the drag force $-\alpha\mathbf{v}$ carries a velocity dependencd, it is reasonable to assume that fluctuation force is independent of velocity, i.e. $\langle R_i v_j \rangle = 0$ for all cartesian indices i and j. In the following, we attempt to justify the physical motivation for the Langevin equation and determine the relationship between the drag coefficient α and the

random force R [37]. From the Langevin equation Eq. (2.12) we can compute the velocity autocorrelation function. Note that we continue to use only one dimension for simplicity. We begin by multiplying by $(e^{\alpha t/m})/m$

$$\dot{v}(t)e^{\alpha t/m} + \frac{\alpha}{m}v(t)e^{\frac{\alpha t}{m}} = \frac{F}{m}e^{\frac{\alpha t}{m}},$$

and integrate from $t = -\infty$. By the use of integration by parts on the latter term on the left-hand side we calculate the velocity

$$\int_{-\infty}^{t} dt' \; \dot{v}(t')e^{\frac{\alpha t'}{m}} + \frac{\alpha}{m}v(t)e^{\frac{\alpha t'}{m}} = \int_{-\infty}^{t} dt' \; e^{\frac{\alpha t'}{m}}\frac{F(t')}{m}$$

$$\int_{-\infty}^{t} dt' \; \dot{v}(t')e^{\frac{\alpha t'}{m}} + \left(\left[v(t')e^{\frac{\alpha t'}{m}}\right]_{-\infty}^{t} - \int_{-\infty}^{t} dt' \; \dot{v}(t')e^{\frac{\alpha t'}{m}}\right) = \int_{-\infty}^{t} dt' \; e^{\frac{\alpha t'}{m}}\frac{F(t')}{m}$$

$$v(t) = \int_{-\infty}^{t} dt' \; e^{\frac{-\alpha(t-t')}{m}}\frac{F(t')}{m},$$

where $e^{\frac{-\alpha t}{m}}$ plays the role of a response function. We can then calculate the autocorrelation

$$\langle v(t)v(0)\rangle = \int_{-\infty}^{t} dt_1 \int_{-\infty}^{0} dt_2 \; e^{\frac{t-t_1-t_2}{m}}\frac{\langle F(t_1)F(t_2)\rangle}{m^2}$$

$$= \int_{-\infty}^{t} dt_1 \int_{-\infty}^{0} dt_2 \; e^{\frac{t-t_1-t_2}{m}}\frac{a\delta(t_1-t_2)}{m^2}$$

$$= \int_{-\infty}^{0} dt_2 \; e^{\frac{t-2t_2}{m}}\frac{a}{m^2} = \frac{a}{2m\alpha}e^{-\frac{\alpha t}{m}},$$

where we used Eq. (2.15) and the fact that the integration commutes with the average (we are allowed to flip the order). By comparing this with the equipartition theorem we get

$$\frac{1}{2}m\langle v^2\rangle = \frac{k_BT}{2}$$

$$\frac{1}{2}m\langle v(0)v(0)\rangle = \frac{a}{4\alpha} = \frac{k_BT}{2}$$

$$a = 2\alpha k_BT$$

We notice the appearance of α meaning that the magnitude of the fluctuations increase both with friction and temperature. Moreover, we can integrate the velocity over time to get displacement $x(t)$ and show that the variance is

$$\langle x^2(t)\rangle = \frac{2k_BT}{\alpha}\left(t - \frac{m}{\alpha}\left(1 - e^{-\alpha t/m}\right)\right).$$

For $t \gg m/\alpha$ only the t-term will survive yielding

$$\langle x^2(t)\rangle = 2k_BTt/\alpha.$$

In 1D, the diffusion constant D is related to the variance as $\langle x^2\rangle = 2Dt$, meaning that this represents the einstein relation $D = \mu k_BT$ with the mobility $\mu = 1/\alpha$.

When $t \ll m/\alpha$ we use the Taylor expansion $1 - e^{-x} \approx x - x^2/2$ for $x \ll 1$ which give

$$\langle x^2(t)\rangle = \frac{k_BT}{m}t^2.$$

Using $\langle x^2\rangle/t^2 = \langle v^2\rangle$ we see that the result is in agreement with the equipartition theorem Eq. (2.13)

$$\langle v^2(t)\rangle = \frac{k_BT}{m} \iff \frac{1}{2}m\langle v^2\rangle_{\text{eq}} = \frac{k_BT}{2}.$$

Thus, we find the finite correlation time α/m to describe the crossover from the ballistic regime $\sqrt{\langle x^2(t)\rangle} \propto \sqrt{t}$ at $t \ll m/\alpha$ to the diffusive regime $\sqrt{\langle x^2(t)\rangle} \propto \sqrt{t}$ at $t \gg m/\alpha$. That is, at short time scales the thermal movement can be thought of as relatively free with a low collision rate, while at longer time scales the movement is characterized by a jittery random-walk-looking motion that is related to diffusion.

2.3.2   Implementing Langevin

The numerical implementation of the Langevin equation Eq. (2.12) is done through the simulation software LAMMPS (see Sec. 2.5) following [38] by defining the force vector for each particle as

$$\mathbf{F} = \mathbf{F_c} + \mathbf{F}_f + \mathbf{F}_r$$
$$= -\nabla U - \gamma m \mathbf{v} + \sqrt{\frac{2k_B T m \gamma}{\Delta t}} \mathbf{h}(t) \tag{2.16}$$

where $\mathbf{F_c}$ is the added conservative force computed via the usual interatomic interactions described by the potential U, $\mathbf{F}_f$ is the drag force described as a damping term $-\gamma m \mathbf{v}$ with $\alpha = \gamma m$, and $\mathbf{F}_r$ is the random fluctuation force where $\mathbf{h}$ is a random vector is drawn from a normal distribution with zero mean and unit variance. The fact that Δt now appears in the denominator for the random force variance $2k_B T m \gamma / \Delta t$ is due to the discretization of time. By applying Eq. (2.16) we get the refined velocity verlet scheme

$$\mathbf{v}_i(t + \Delta t/2) = \mathbf{v}_i(t) - \frac{\Delta t}{2} \left(\frac{\nabla_i U(t)}{m_i} + \gamma \mathbf{v}_i \right) + \sqrt{\frac{k_B T \gamma \Delta t}{2m_i}} \mathbf{h}_i$$
$$\mathbf{r}_i(t + \Delta t) = \mathbf{r}_i(t) + \mathbf{v}_i(t + \Delta t/2)\Delta t$$
$$\mathbf{v}_i(t + \Delta t) = \mathbf{v}_i(t + \Delta t/2) - \frac{\Delta t}{2} \left(\frac{\nabla_i U(t + \Delta t)}{m_i} + \gamma \mathbf{v}_i(t + \Delta t/2) \right) + \sqrt{\frac{k_B T \gamma \Delta t}{2m_i}} \mathbf{h}_i$$

with new random vector $\mathbf{h}_i$ for each particle and each update. Notice however, we will only apply the thermostat to specific regions in our simulation, mainly on the outer edges, while the main part of interest is modeled exclusively by Newton's equation of motion as described in Eq. (2.7). This is done in order to avoid affecting the governing parts of the friction simulation to much. We use a damping of $1/\gamma = m/\alpha = 1\,\mathrm{ps}$ as a common default choice.

2.4   Limitations

On a general note, MD simulations are limited to relatively small time and size scales due to the available computation time. Morden CPUs perform on the order of 10^9 floating-point operations per second (FLOPS) per core [22]. MD simulations can benefit from medium-scale parallelization, demonstrating relatively linear scaling up to around 10^2 cores, providing roughly 10^{11} FLOPS. In a typical MD calculation, the computation of the force acting on each atom, which can be the most time-consuming step depending on the complexity and range of the force field, requires N_{step} being approximately 10 to 10^2 FLOPS. Therefore, for a typical simulation size of $N = 10^5$ atoms with a timestep in the fs range, we find the ratio of simulated time to real-time on the order

$$\frac{\mathrm{FLOPS}}{N \cdot N_{\mathrm{step}} \cdot dt^{-1}} = \frac{10^{11}}{10^5 \cdot 10 \cdot 10^{15}} = 10^{-10}.$$

Hence, the simulation can make progress at a rate of 10^5 fs per second, or roughly $10^9\,\mathrm{fs} = 1\,\mu\mathrm{s}$ per day. For the realism of the simulations, some of the weakness includes the lack of quantum effects and a reduction in the number of dissipation channels available

2.5   LAMMPS

For the implementation of our MD we will use LAMMPS (Large-scale Atomic/Molecular Massively Parallel Simulator) [39]. LAMMPS provides a numerical framework for setting up the system and integrating the equations of motion with easy access to parallelized simulations. This essentially allows us to focus on the higher-level features of the numerical procedure rather than building the simulation from scratch.

Part II

Simulations

Chapter 3

Summary

In this thesis we have studied nanoscale friction of a Kirigami graphene sheet under the influence of load and strain using MD simulations. We have developed a numerical framework for generating various Kirigami designs which was used to create a dataset of the frictional behavior depending on the Kirigami pattern, strain and loading. Our findings suggest that the frictional behavior of a Kirigami sheet is highly dependent on the geometry of the pattern and the strain conditions. We observed that the out-of-plane buckling can be associated with a non-linear friction-strain curve which can be utilized to demonstrate a negative friction coefficeint in a system with coupled load and strain. Moreover, we have investigated the possibility to use machine learning on this dataset and attempted an accelerated search. Our result suggest that machine learning can be feasible for this approach, but more data is needed to provide a more reliable foundation for a search of new Kirigami patterns. In this chapter we will summarize the findings in more detail and draw some conclusions. At the end we will provide some topics for further research.

3.1   Summary and conclusions

3.1.1   Designing an MD simulation

We have designed an MD simulation for the examination of friction for a graphene sheet sliding on a silicon substrate. The key system features were the introduction of the pull blocks, defined as the end regions of the sheet with respect to the sliding direction, which was utilized for applying normal load and sliding the sheet. The pull blocks were made partly rigid and used to employ a thermostat as well. By an analysis of the friction forces retrieved from sliding simulations we defined a standardized metric for kinetic friction. We measured the force acting from the substrate on the full sheet (including the pull blocks) with respect to the sliding direction and defined kinetic friction by the mean value of the last half of the simulation. The uncertainties were estimated on the basis of the fluctuations in the running mean. We found that the assessment of static friction was ambiguous for our simulation and did not pursue this further. From the analysis of the force traces, friction force vs. time, we identify the friction behavior in our simulation domain as being in the smooth sliding regime mainly due to the choice of sliding speed ($20\,\mathrm{m/s}$) and infintely stiff springs. This was further supported by a demonstration of a transition to stick-slip behavior with softer springs and a lowering of sliding speed. By conducting a more systematic investigation of the effects of temperature, sliding speed, spring constant and timestep, we settled on the default values based on numerical stability and computational cost. We found that friction increased with temperature which we attribute to being in the ballistic sliding sliding regimem. We used the room temperature $300\,\mathrm{K}$ as a standard choice. Furthermore, we found friction to increase with velocity as expected, with some signs of phonon resonance at certain sliding speeds as well. We chose a rather high velocity of $20\,\mathrm{m/s}$ mainly for the consideration of computational costs. For the spring constant, we found decreasing friction with increasing stiffness of the springs which is associated with the transition from a stick-slip-influenced regime toward smooth sliding. The choice of an infintely stiff spring was made from a stability assessment. Finally, we confirmed that a timestep of $1\,\mathrm{fs}$ provides reasonable numerical stability. However, based on fluctuations with timestep we find that the uncertainty in the simulations might be higher than first estimated.

3.1.2   Generetig Kirigami patterns

In order to invstigate the effects of Kirigami design we have created a numerical framework for generating various patterns. By defining an indexing system for the hexagonal lattice structure we were able to define the Kirigami designs as a 2D binary matrix for numerical implementation. We digitalized two different macroscale designs, which we named the *Tetrahedron* and *Honeycomb* pattern, that successfully produced out-of-plane buckling when stretched. Through our numerical framework we were able to create an ensemble of perturbed unique variations which yielded approximately 135k and 2025k for the Tetrahedron and Honeycomb patterns respectively. When considering the possibility to translate the patterns we find the ability to increase the number by roughly a factor 100. In addition we created a framework for generating random walk based Kirigami patterns. This was regulated by introducing features such as bias, avoidance of existing cuts, preference to keeping a direction and procedures to repairing the sheet for simulation purposes. In general, the capabilities of the numerical framework for generating Kirigami designs exceeded our computational resources with regard to performing MD simulation under different load and strain for each of the designs. Thus our MD-based dataset only utilized a subset of configurations with 9660 data points based on 216 Kirigami configurations (Tetrahedron: 68, Honeycomb: 45, Random walk: 100, Pilot study: 3). Thus our Kirigami generative framework can be valuable for further studies on an extended dataset.

3.1.3   Control friction using Kirigami

We have investigated the frictional behavior of the Tetrahedron and Honeycomb patterns in comparison to a non-cut sheet under various strains and loads. Initially, we observed that straining the Kirigami sheets in vacuum resulted in an out-of-plane buckling. When adding the substrate to the simulation this translated into a decreasing contact area with strain. We found the Honeycomb sheet to exhibit the most significant buckling with a corresponding reduction of relative contact area to approximately 43%. The non-cut sheet did not produce any significant buckling in comparison. We found that friction generally increased with strain which contradicts the asperity theory hypothesis of decreasing friction with decreasing contact area. Moreover, the friction-strain curve exhibited highly non-linear trends with strong negative slopes (see **??**), while the non-cut sheet did not show any significant dependency on the strain We also found that the non-stretched Kirigami patterns did affect friction to some degree, but this was one order of magnitude lower than the effects associated with the strain in combination. This led us to the conclusion that the changing contact area cannot be regarded as a dominant mechanism for friction in the Kirigami sheet system nor the independent consideration of sheet configuration or tension in the sheet. When considering the dependency with load we generally found a weak dependency which can be associated with a friction coefficient on the order of 10^{-4}–10^{-5} even though we could not confirm any clear relationship. This is best attributed to a superlubric state of the graphene sheet as seen in other studies as well. The slope of the friction-load curves was not considerably affected by the straining of the Kirigami sheet which led us to the conclusion that the strain-induced effects are dominant in comparison to any load-related effects. By proposing a linear coupling between load and strain with ratio R we find that these results suggest the possibility to find negative friction coefficients in certain load ranges following $-R12.75\,\text{nN}$ for the Tetrahedon and $-R \cdot 2.72\,\text{nN}$ for the Honeycomb pattern.

3.1.4   Capture trends with machine learning

The dataset reveals some general correlations with mean friction, such as a positive correlation to strain (0.77) and porosity (0.60), and a negative correlation to contact area (-0.67). These results align with the finding in the pilot study, suggesting that the change in friction is associated with cuts in the sheet (porosity) and a changing contact area.

By defining the friction property metrics: $\min F_{\text{fric}}$, $\max F_{\text{fric}}$, $\max \Delta F_{\text{fric}}$ and max drop (maximum decrease in friction with strain), we investigated the top candidates within our dataset. From these results, we found no incentive for the possibility to reduce friction with the Kirigami approach since the non-cut sheet provided the lowest overall friction. Regarding the maximum properties, we found an improvement from the original pilot study values and with the Honeycomb pattern producing the highest scores. This suggests that the data contains some relevant information for optimization with respect to these properties. Among the top candidates, we found that a flat friction-strain profile is mainly associated with little decrease in the contact area and vice versa which again aligns with the pilot study findings.

For the machine learning investigation, we have implemented a VGGNet-16-inspired convolutional neural network with a deep "stairlike" architecture: C32-C64-C128-C256-C512-C1024-D1024-D512-D256-D128-D64-D32, for convolutional layers C with the number denoting channels and fully connected (dense) layers D with the number denoting nodes. The final model contains 1.3×10^7 parameters and was trained using the ADAM optimizer for a cyclic learning rate and momentum scheme. We trained the network for a 1000 epochs while saving the best model during training based on the validation score. The model validation performance gives a mean friction R^2 score of $\sim 98\%$ and a rupture accuracy of $\sim 96\%$. However, we got lower scores for a selected subset of the Tetrahedon ($R^2 \sim 88.7\%$) and Honeycomb ($R^2 \sim 96.6$) pattern based on the top 10 max drop scores respectively. These scores were lower despite the fact that the selected set was partly included in the training data as well in addition to the fact that the hyperparameter selection favored the performance on this selected set as well. Thus we conclude that these selected configurations, associated with a highly non-linear friction-strain curve, represent a bigger challenge for the machine learning prediction. One interpretation is that these involve the most complex dynamics and perhaps that this is not readily distinguished from the behavior of the other configurations which constitute the majority of the data set. By evaluating the ability of the model to rank the dataset according to the property scores we found in general a good representation of the top 3 scores for the maximum categories, while the minimum friction property ranking was lacking. We attribute this latter observation to a higher need for precision which the model did not possess.

In order to provide a more true evaluation of the model performance we created a test set based on MD simulations for an extended Random walk search. This test revealed a significantly worse performance than seen for the validation set with a two-order of magnitude higher loss and a negative friction mean R^2 score which corresponds to the prediction being worse than simply guessing on the true data mean. However, by reconsidering the choice of architecture complexity hypertuning with respect to the validation loss, we found similar poor results on the test set. This indicates, that the test score is not simply a product of a biased hypertuning process but instead points to the fact that our original dataset did not cover a wide enough configuration distribution to accurately capture the full physical complexity of the Kirigami friction behavior. Based on the validation scores we conclude that the use of machine learning is feasible, but that we need to improve the dataset in order to reach a reliable model.

3.1.5 Accelerated search

Using the ML model we performed two types of accelerated search. One by evaluating the property scores of an extended dataset and another with the use of the genetic algorithm approach. For the extended dataset search, we used the developed pattern generators to generate $135\,\text{k} \times 10$ Tetrahedon, $2025\,\text{k} \times 10$ Honeycomb and $10\,\text{k}$ Random walk patterns. For the minimum friction property, the search suggests a favoring of a low cut density (low porosity) which aligns with the overall idea that the dataset does not provide an incentive for further friction reduction with the non-cut sheet resulting in the lowest friction. The maximum properties resulted in some minor score increases but the suggested candidates were mainly overlapping with the original dataset. By investigating the model prediction sensitivity to the translation of the Tetrahedron and Honeycomb patterns we found that the model predictions varied drastically with small translations. This can be attributed to a physical dependency since the edge of the sheet is affected by this translation. However, due to the poor model performance on the test set, we find it more likely to be a model insufficiency related to the lacking dataset.

For the genetic algorithm approach, we investigated the optimization for the max drop property using starting population based on the result from the extended dataset accelerated search, and some random noise initializations with different porosity values. This approach did not provide any noteworthy incentive for new design structures worth more investigation. In general, the initialization of the population itself proved to be a more promising strategy than the genetic algroithm. However, this is highly affected by the uncertainty of the model predictions, and thus we did not pursue this any further. By considering the Grad-CAM explanation method we found that the model predictions occasionally payed considerable attention to the top and bottom edge of the configurations. This is surprising since these are not true edges but are connected to the pull blocks in the simulation. Despite the uncertainties in the predictions, we argue that this might be attributed to thermostat effects from the pull blocks and thus we note this as a feature worth investigating in the simulations.

3.1.6   Negative friction coefficient

By enforcing a coupling between load and sheet tension, mimicking a nanomachine attached to the sheet, we investigated the load curves arising from the loading of the Tetrahedron $(7, 5, 1)$ and Honeycomb $(2, 2, 1, 5)$ pattern from the pilot study. The non-linear trend observed for increasing strain carried over to the coupled system as well producing a highly non-linear friction-load curve. The Honeycomb pattern exhibited additionally a non-linear strain-tension curve which resulted in an almost discontinuous increase in friction for the initial increase in load. We attribute this feature to an unfolding process visually confirmed from the simulation frames. For the coupled system with a load-to-tension ratio of 6 we found regions in the friction-load curve with significant negative slopes. By considering the maximum and minimum points for such regions we estimated the average friction coefficient to be -0.31 in the range $F_N = [4.65, 6.55]$ nN for the Tetrahedron pattern and -0.38 in the range $F_N = [0.71, 4.31]$ nN for the Honeycomb pattern. .

Our findings suggest that the combined use of Kirigami cuts and strain has considerable potential for friction control, especially under the influence of a coupled system of load and strain.

3.2   Outlook

In this thesis, we have successfully shown that certain Kirigami designs exhibit non-linear behavior with strain. This discovery was done through a focus on the exploration of the effects of different designs. This invites further investigation of the underlying mechanisms behind this phenomenon. By considering one or two design, based on Tetrahedron and Honeycomb patterns, it would be valuable to investigate the effects on the friction-strain curve under various physical parameters.

First of all, we suggest an investigation of how the friction-strain curve depends on temperature, sliding speed, spring constant, and loads for an increased range $F_N > 100nN$. This is especially interesting in the context of physical conditions leading to a stick-slip behavior since our study takes a basis in smooth sliding friction. Moreover, it would be valuable to verify that the choices for relaxation time, pauses, interatomic potentials and substrate material are not critical for the qualitative observations. Especially the Adaptive Intermolecular Reactive Empirical Bond Order (AIREBO) potential for the modeling of the graphene sheet might be of interest. In this context, it might also be useful to investigate the effects of excluding adhesion in the simulations. In order to gain further insight into the role of commensurability one could vary the scan angle as well. Since we suspect that our simulation corresponds to a incommensurable superlubric state, certain scan angles is hypothesized to yield higher friction. If the friction-strain curve is based on a commensurability effect this might yield qualitative different results and perhaps also allowing for a lowering of friction with strain. We might also consider investigating the friction-strain relationship under a uniform load to get insight into how the loading distribution effects the out-of-plane buckling and associated frictional effects.

Another topic worth studying is the relation to scale and edge effects. This includes an investigation of scaling effects, considering the ratio of the sheet to the edge, but also a translation of the sheet patterns to study the presence of any Kirigami-induced edge effects. The latter is motivated by the findings from the machine learning predictions. With this regard, we would also suggest a more detailed study of the effect of the thermostat in the pull blocks which is suggested to have a possibly importance when judging from the Grad-CAM analysis.

For the machine learning approach, our findings suggest that the dataset is extended considerably. This can be done with respect to the aim of exploring Kirigami configurations as done in this thesis, but it can also be done for a single configuration under variation of some of the simulation parameters to support some of the above mentioned investigations. In that context, one could consider more advanced model architectures and machine learning techniques. If successful this would invite further studies of inverse design methods such as GAN or diffusion models.

Appendices

Appendix A

Appendix A

Appendix A

Appendix B

Appendix B

Appendix C

Bibliography

[1] E. Gnecco and E. Meyer, *Elements of friction theory and nanotribology* (Cambridge University Press, 2015).

[2] Bhusnan, "Introduction", in *Introduction to tribology* (John Wiley & Sons, Ltd, 2013) Chap. 1, 1–?

[3] H.-J. Kim and D.-E. Kim, "Nano-scale friction: a review", International Journal of Precision Engineering and Manufacturing **10**, 141–151 (2009).

[4] K. Holmberg and A. Erdemir, "Influence of tribology on global energy consumption, costs and emissions", Friction **5**, 263–284 (2017).

[5] B. Bhushan, "Gecko feet: natural hairy attachment systems for smart adhesion – mechanism, modeling and development of bio-inspired materials", in *Nanotribology and nanomechanics: an introduction* (Springer Berlin Heidelberg, Berlin, Heidelberg, 2008), pp. 1073–1134.

[6] P. Z. Hanakata, E. D. Cubuk, D. K. Campbell, and H. S. Park, "Accelerated search and design of stretchable graphene kirigami using machine learning", Phys. Rev. Lett. **121**, 255304 (2018).

[7] P. Z. Hanakata, E. D. Cubuk, D. K. Campbell, and H. S. Park, "Forward and inverse design of kirigami via supervised autoencoder", Phys. Rev. Res. **2**, 042006 (2020).

[8] L.-K. Wan, Y.-X. Xue, J.-W. Jiang, and H. S. Park, "Machine learning accelerated search of the strongest graphene/h-bn interface with designed fracture properties", Journal of Applied Physics **133**, 024302 (2023).

[9] Y. Mao, Q. He, and X. Zhao, "Designing complex architectured materials with generative adversarial networks", Science Advances **6**, eaaz4169 (2020).

[10] Z. Yang, C.-H. Yu, and M. J. Buehler, "Deep learning model to predict complex stress and strain fields in hierarchical composites", Science Advances **7**, eabd7416 (2021).

[11] A. E. Forte, P. Z. Hanakata, L. Jin, E. Zari, A. Zareei, M. C. Fernandes, L. Sumner, J. Alvarez, and K. Bertoldi, "Inverse design of inflatable soft membranes through machine learning", Advanced Functional Materials **32**, 2111610 (2022).

[12] S. Chen, J. Chen, X. Zhang, Z.-Y. Li, and J. Li, "Kirigami/origami: unfolding the new regime of advanced 3D microfabrication/nanofabrication with "folding"", Light: Science & Applications **9**, 75 (2020).

[13] Z. Deng, A. Smolyanitsky, Q. Li, X.-Q. Feng, and R. J. Cannara, "Adhesion-dependent negative friction coefficient on chemically modified graphite at the nanoscale", Nature Materials **11**, 1032–1037 (2012).

[14] B. Liu, J. Wang, S. Zhao, C. Qu, Y. Liu, L. Ma, Z. Zhang, K. Liu, Q. Zheng, and M. Ma, "Negative friction coefficient in microscale graphite/mica layered heterojunctions", Science Advances **6**, eaaz6787 (2020).

[15] D. Mandelli, W. Ouyang, O. Hod, and M. Urbakh, "Negative friction coefficients in superlubric graphite–hexagonal boron nitride heterojunctions", Phys. Rev. Lett. **122**, 076102 (2019).

[16] R. W. Liefferink, B. Weber, C. Coulais, and D. Bonn, "Geometric control of sliding friction", Extreme Mechanics Letters **49**, 101475 (2021).

[17] Y. Dong, A. Vadakkepatt, and A. Martini, "Analytical models for atomic friction", Tribology Letters **44**, 10.1007/s11249-011-9850-2 (2011).

[18] N Manini, O. M. Braun, E Tosatti, R Guerra, and A Vanossi, "Friction and nonlinear dynamics", Journal of Physics: Condensed Matter **28**, 293001 (2016).

[19] B. Bhushan, "Nanotribology and nanomechanics", Wear **259**, 15th International Conference on Wear of Materials, 1–? (2005).

[20]P. Carloni, U. Rothlisberger, and M. Parrinello, "The Role and Perspective of Ab Initio Molecular Dynamics in the Study of Biological Systems", Accounts of Chemical Research **35**, Publisher: American Chemical Society, 455–464 (2002).

[21]P. Hohenberg and W. Kohn, "Inhomogeneous electron gas", Phys. Rev. **136**, B864–B871 (1964).

[22]A. Vanossi, N. Manini, M. Urbakh, S. Zapperi, and E. Tosatti, "Modeling friction: from nanoscale to mesoscale", Reviews of Modern Physics **85**, 529–552 (2013).

[23]S. Li, Q. Li, R. W. Carpick, P. Gumbsch, X. Z. Liu, X. Ding, J. Sun, and J. Li, "The evolving quality of frictional contact with graphene", Nature **539**, Number: 7630, 541–545 (2016).

[24]J. Tersoff, "New empirical approach for the structure and energy of covalent systems", Phys. Rev. B **37**, 6991–7000 (1988).

[25]P. Zhu and R. Li, "Study of nanoscale friction behaviors of graphene on gold substrates using molecular dynamics", Nanoscale Research Letters **13**, 34 (2018).

[26]Q. Zhang, D. Diao, and M. Kubo, "Nanoscratching of multi-layer graphene by molecular dynamics simulations", Tribology International **88**, 85–88 (2015).

[27]H. M. Yoon, Y. Jung, S. C. Jun, S. Kondaraju, and J. S. Lee, "Molecular dynamics simulations of nanoscale and sub-nanoscale friction behavior between graphene and a silicon tip: analysis of tip apex motion.", Nanoscale **7 14**, 6295–303 (2015).

[28]S. Corporation, *Pair_style lj/cut command*, (Dec. 22, 2022) `https://docs.lammps.org/pair_lj.html`.

[29]X. Wang, S. Ramírez-Hinestrosa, J. Dobnikar, and D. Frenkel, "The lennard-jones potential: when (not) to use it", Phys. Chem. Chem. Phys. **22**, 10624–10633 (2020).

[30]R. Naeem, *Lennard-jones potential*, (Nov. 25, 2022) `https://chem.libretexts.org/Bookshelves/Physical_and_Theoretical_Chemistry_Textbook_Maps/Supplemental_Modules_(Physical_and_Theoretical_Chemistry)/Physical_Properties_of_Matter/Atomic_and_Molecular_Properties/Intermolecular_Forces/Specific_Interactions/Lennard-Jones_Potential`.

[31]S. Corporation, *Pair_style sw command*, (Dec. 22, 2022) `https://docs.lammps.org/pair_sw.html`.

[32]F. H. Stillinger and T. A. Weber, "Computer simulation of local order in condensed phases of silicon", Phys. Rev. B **31**, 5262–5271 (1985).

[33]S. Corporation, *Pair_style tersoff command*, (Dec. 22, 2022) `https://docs.lammps.org/pair_tersoff.html`.

[34]J. Tersoff, "Modeling solid-state chemistry: interatomic potentials for multicomponent systems", Phys. Rev. B **39**, 5566–5568 (1989).

[35]W. Commons, *File:bond-order interatomic potential.png — wikimedia commons, the free media repository*, [Online; accessed 02/05/2023], 2023.

[36]D. Frenkel and B. Smit, *Understanding molecular simulation: from algorithms to applications*, Second, Vol. 1, Computational Science Series (Academic Press, San Diego, 2002).

[37]F. Ravndal and E. G. Flekkøy, *Statistical physics– a second course*, Department of Physics, University of Oslo, 2019.

[38]T. Schneider and E. Stoll, "Molecular-dynamics study of a three-dimensional one-component model for distortive phase transitions", Phys. Rev. B **17**, 1302–1322 (1978).

[39]A. P. Thompson, H. M. Aktulga, R. Berger, D. S. Bolintineanu, W. M. Brown, P. S. Crozier, P. J. in 't Veld, A. Kohlmeyer, S. G. Moore, T. D. Nguyen, R. Shan, M. J. Stevens, J. Tranchida, C. Trott, and S. J. Plimpton, "LAMMPS - a flexible simulation tool for particle-based materials modeling at the atomic, meso, and continuum scales", Comp. Phys. Comm. **271**, 108171 (2022).